IOP Publishing Physica Scripta
Phys. Scr. 95 (2020) 055813 (10pp) https://doi.org/10.1088/1402-4896/ab7a39

Structural and spectroscopic studies of nanocrystalline $Ni_{1-x}Mg_xFe_2O_4$ ferrites synthesized by a microwave-assisted combustion route

Abdulaziz Abu El-Fadl[1], **Azza M Hassan and Mohamed A Kassem**[1]

Physics Department, Faculty of Science, Assiut University, 71516 Assiut, Egypt

E-mail: abulfadla@yahoo.com and makassem@aun.edu.eg

Received 14 December 2019, revised 16 February 2020
Accepted for publication 26 February 2020
Published 13 March 2020

Abstract

In this work, the synthesis of $Ni_{1-x}Mg_xFe_2O_4$ ($0 \leqslant x \leqslant 1.0$) nanoparticles by a facile microwave-assisted combustion method is reported with detailed study of the structural and optical properties. By employing techniques of x-ray diffraction (XRD) with Rietveld refinement, transmission electron microscope (TEM, HRTEM, TEM-EDX), Fourier transform infrared spectroscopy (FTIR) and UV-Visible spectroscopy, the synthesized nanoparticles are characterized and introduced for further study of size-confined properties. Nanocrystals of a pure cubic spinel structured phase with average particle size of 20–40 nm were successfully synthesized in the whole range of x. In consistence with Vegard's law for a solid solution lattice, the lattice constant increases linearly with the substitution for Ni^{2+} with the relatively larger Mg^{2+} cations. The Rietveld analysis of the observed XRD patterns reveals an inversed spinel structure in $NiFe_2O_4$ nanoparticles with a decreased inversion factor by Mg-substitution. The results of UV-Visible absorbance indicate a wide energy gap of about 3.6 eV for $NiFe_2O_4$ nanoparticles thatmonotonically tuned towards a narrow band gap by Mg-doping.

Keywords: spinel ferrites, microwave combustion, XRD, TEM, optical properties, energy gap tuning, nanoparticles

(Some figures may appear in colour only in the online journal)

1. Introduction

Spinel ferrites with a general formula of MFe_2O_4 (M is a divalent metal cation such as Mg^{2+}, Co^{2+}, Ni^{2+}, Cu^{2+} and Zn^{2+}, locates completely in the tetrahedral A^{IV}-sites fora normal spinel structure) have attracted much attention due to the interesting properties wich make them useful in a vast range of technological applications [1–5]. The physical properties of spinel ferrites are dependent on the cations distribution, oxygen vacancy and particle size which all are influenced by the employed synthesis route. Furthermore, substitutions among the M divalent cations or by a trivalent cation (Cr^{3+}, Mn^{3+}, Al^{3+}, Ga^{3+} etc) can easily modify the magnetic, dielectric and optical properties of nanostructured ferrites [6–12]. For example, the chemical and physical properties of $NiFe_2O_4$ can be enhanced by substitution with divalent ions such as Zn^{2+}, Co^{2+}, Cu^{2+} and Mg^{2+} for Ni^{2+} [13–16]. Pure Ni-ferrite has been widely investigated as a candidate for magnetic devices, catalysis in chemical reactions and for drug delivery in biomedicine [17–19]. Incorporation of the nonmagnetic Mg^{2+} ion into the composition of Ni-ferrite makes it promising for further novel technological applications including electromagnetic interference shielding [20], effective photocatalytic performance compared to pure Ni-ferrites [21], anode material for rechargeable batteries [22] and a good Antibacterial in biomedicine [17].

Due to the synthesis-routes dependence of the nanoparticles properties, many novel synthesis routes such as the

[1] Authors to whom any correspondence should be addressed.

co-precipitation [23], hydrothermal [24] and sol–gel [25] methods have been developed in the last decades to prepare nanocrystalline spinel ferrites. The microwave assisted combustion method has been recently developed and gained much interest as it is simple, cost effective and productive method [26]. It requires raw materials which are mostly available including metal salts, as sources for metal elements and an organic compound (e.g. glycine, urea, citric acid, alanine or carbohydras) as a fuel. In this process, the microwave energy provides a rapid uniform heating at the molecular level, by the induced motion of molecules inside the material reactants, which is required to increase nucleation rather than growth of the synthesized particles. It produces homogenous nanocrystalline particles with a high yield within few minutes in contrast to other conventional synthesis routes which use an external source of heat (hot plate or muffle oven) and mostly require longer time resulting in relatively larger particle size.

The present work aims to synthesis Mg-substituted Ni-ferrite nanoparticles of high crystallinity, by using a facile microwave combustion method. The synthesized phase and composition are identified by the XRD Rietveld analysis, FTIR, TEM and EDX measurements. The microstructure, crystallinity, particles shape and size are investigated by TEM and HRTEM and the effect of Mg^{2+} substitution on the structure and optical energy gap of Ni ferrite nanoparticles is studied in detail.

2. Experimental techniques

2.1. Materials and synthesis

Ferrite nanoparticles with the composition of $Ni_{1-x}Mg_xFe_2O_4$ ($x = 0.0 - 1.0$ in a step of 0.1) were prepared using the microwave combustion method described here. Hydrated metal nitrates $Mg(NO_3)_2.6H_2O$, $Ni(NO_3)_2.6H_2O$ and $Fe(NO_3)_3.9H_2O$ were used and dissolved in the appropriate ratio with the glycine ($(NH_2)_2COOH$) fuel in a least amount of distilled water. The produced solution was introduced into a microwave oven (Olympic electric, KOR-6Q1B) operating at a maximum power of 800 W for 20 min. A voluminous and fluffy product that grades in colour from black to brown with increasing the Mg content was produced. The product was easily ground to fine powders for further characterization and prepared for measurements.

2.2. Characterization and measurements

The synthesized phases were identified by the powder x-ray diffraction (XRD) technique using a diffractometer (Philips PW1710, Netherlands) equipped with an automatic divergent slit and CuK_α-radiation ($\lambda = 0.154\,18$ nm) produced by a graphite monochromator. FTIR spectroscopy have been performed on the samples using NICOLET FTIR 6700 spectrometer by employing the KBr pellet method, in the range 400–4000 cm^{-1}.

The microstructure as well as average particles size, shape and crystallinity have been investigated by the (high-resolution) transmission electron microscopy (HR)TEM using a JEOL JEM-2100F electron microscope. An attached unit of energy dispersive x-ray spectroscopy (EDX-TEM) has been employed to investigate the elemental compositions. The chemical composition is averaged for the investigation results for many particles in the measured samples.

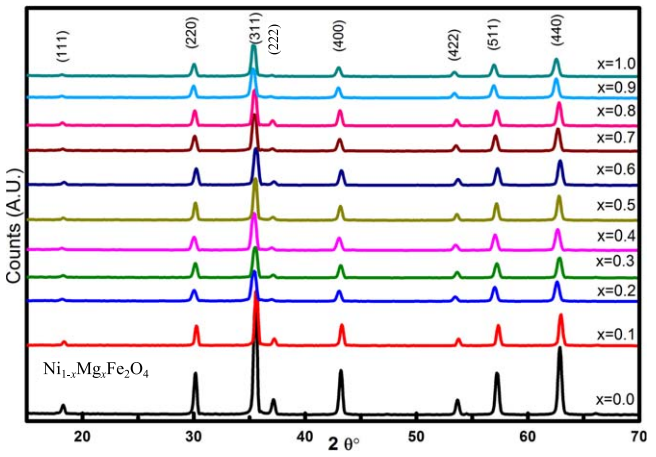

Figure 1. XRD patterns of $Ni_{1-x}Mg_xFe_2O_4$ nanoparticles measured at room temperature.

The optical absorbance has been measured using a Thermo Evolution 300 UV-Visible Spectrophotometer. The absorbance spectra have been collected from a suspension of 1-mg powder sample, added and sonicated for 10 min. in 10 ml of the DMSO solvent, in a wavelength range of 200–900 nm.

3. Results and discussion

3.1. Structural properties and crystallite size

Typical XRD patterns of the synthesized Ni-Mg ferrite nanopowders are shown in figure 1. All the detected peaks of Mg-Ni ferrite system are solely indexed with the spinel crystal structure with the space group $Fd\bar{3}m$ in a good accordance with the standard ICDD cards, No. 04-015-7027 for Mg ferrite and No. 04-014-8286 for Ni ferrite. There are no extra diffraction lines of any secondary phases appear over the whole composition range indicating successful synthesis of a mono-phase samples of the spinel cubic structure. Further, the noticed shift of reflection lines to lower Bragg's angle with the increased Mg content indicates successful substitution for Ni^{2+} by Mg^{2+} ions of little larger divalent ions in a solid solution spinel structure.

Figure 2 shows the Rietveld refinement of the experimental XRD patterns by assuming the cubic spinel structure, space group 227 ($Fd\bar{3}m$) setting #2, for selected $Ni_{1-x}Mg_xFe_2O_4$ compositions. The refinement has performed by employing the RIETAN-FP system for pattern-fitting structure refinement [27]. Sites 8a (1/8, 1/8, 1/8) and 16d (½, ½, ½) are assumed for atoms lie in the tetrahedral A^{IV}- and octahedral B^{VI}-sites, respectively, while the site 32e with refined positions ($x = y = z = u$) is for the oxygen atoms. During the Rietveld analysis, the lattice constant (a), oxygen position (u), occupancies of atoms (g) and peaks shape parameters (FWHM, position,

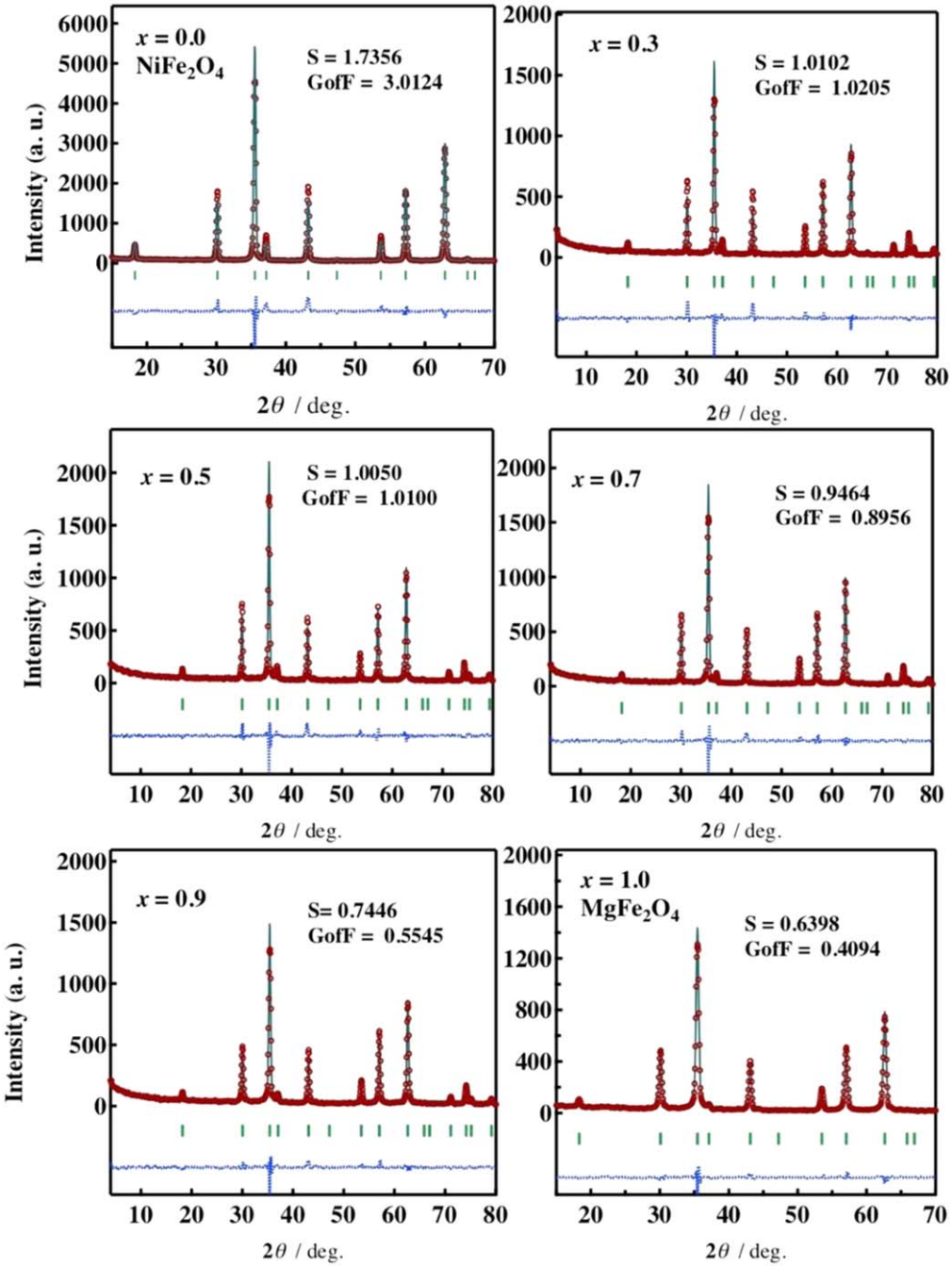

Figure 2. Rietveld refinement of the observed XRD patterns (symbols) of $Ni_{1-x}Mg_xFe_2O_4$ nanoparticles to the cubic spinel structure at Bragg reflection angles shown by the vertical bars. Calculated patterns and their deviations from the experimental patterns are shown by solid and dotted lines, respectively. The corresponding relative reliability factor, $S = R_{\text{weighted-profile}}/R_{\text{expected}}$, and goodness-of-fit indicator, GofF, are shown.

intensity, etc) were refined. The inversed spinel structure is revealed for $NiFe_2O_4$ with an inversion factor $\delta = 0.997$, as shown in table 1, so we assumed Ni completely locate in the B^{VI}-site in the $Ni_{1-x}Mg_xFe_2O_4$ whole series [26]. The refinement resulted in an oxygen position u of about 0.253–0.256 for $Ni_{1-x}Mg_xFe_2O_4$ nanoparticles. All structure parameters derived from the Rietveld analysis are summarized in table 1.

As well as the lattice constant values obtained by the Rietveld analysis of XRD in the whole range of 2θ (table 1), a is further accurately determined through the Nelson-Riley extrapolation method using the positions of high-angle peaks (at $2\theta > 40°$) also obtained from the Rietveld analysis. The values of the apparent lattice constant, $a_{hkl} = \frac{\lambda\,[h^2+k^2+l^2]^{1/2}}{2\sin\theta}$ for a cubic structure, obtained from different diffraction planes are plotted against Nelson-Riley function, $F(\theta) = \frac{\cos^2}{\sin} + \frac{\cos^2}{2}$, and extrapolated to $F(\theta) = 0$ [28]. The obtained values of a for Ni-Mg ferrites nanoparticles are plotted against Mg^{2+} content (x)

Table 1. Rietveld-refined structural parameters of $Ni_{1-x}Mg_xFe_2O_4$ nanoparticles: chemical formula ($A^{IV}B_2^{VI}Fe_2O_4$), inversion factor (δ), lattice parameter (a) and average estimated values of density (ρ_{XRD}), hopping length for the A^{IV}-site (L_A) and B^{VI}-site (L_B), internal lattice strain (ε), crystallite size (d_{XRD}) and TEM-determined particle size (d_{TEM}).

x (Mg^{2+})	$A^{IV}B_2^{VI}O_4$	δ	a (Å)	ρ_{XRD} (g cm^{-3})	L_A (Å)	L_B (Å)	$\varepsilon \times 10^{-4}$	d_{XRD} (nm)	d_{TEM} (nm)
0.0	$(Ni_{0.003}Fe_{0.997})(Ni_{0.499}Fe_{0.501})_2O_4$	0.997(19)	8.318(41)	5.41	3.60	2.941	4.2	32.04	31
0.1	$(Mg_{0.02}Fe_{0.98})(Mg_{0.04}Ni_{0.45}Fe_{0.51})_2O_4$	0.982(37)	8.324(28)	5.32	3.60	2.943	9.2	45.11	
0.2	$(Mg_{0.03}Fe_{0.97})(Mg_{0.085}Ni_{0.4}Fe_{0.515})_2O_4$	0.971(42)	8.329(34)	5.23	3.61	2.945	5.7	25.68	22
0.3	$(Mg_{0.01}Fe_{0.99})(Ni_{0.35}Mg_{0.145}Fe_{0.505})_2O_4$	0.992(18)	8.333(45)	5.11	3.62	2.953	−1.3	22.73	
0.4	$(Mg_{0.045}Fe_{0.955})(Ni_{0.3}Mg_{0.178}Fe_{0.522})_2O_4$	0.955(42)	8.337(34)	5.06	3.61	2.948	1.1	22.73	29
0.5	$(Mg_{0.06}Fe_{0.94})(Ni_{0.25}Mg_{0.22}Fe_{0.53})_2O_4$	0.936(41)	8.344(32)	4.97	3.61	2.950	6.8	37.13	
0.6	$(Mg_{0.078}Fe_{0.922})(Ni_{0.2}Mg_{0.26}Fe_{0.54})_2O_4$	0.922(35)	8.346(37)	4.89	3.61	2.951	−1.2	21.27	27
0.7	$(Mg_{0.098}Fe_{0.902})(Ni_{0.15}Mg_{0.301}Fe_{0.549})_2O_4$	0.902(41)	8.360(36)	4.78	3.62	2.956	13.2	25.41	
0.8	$(Mg_{0.192}Fe_{0.808})(Ni_{0.1}Mg_{0.304}Fe_{0.596})_2O_4$	0.808(36)	8.363(33)	4.70	3.62	2.957	−2.7	20.69	27
0.9	$(Mg_{0.22}Fe_{0.78})(Ni_{0.05}Mg_{0.34}Fe_{0.61})_2O_4$	0.781(36)	8.363(32)	4.62	3.62	2.957	−2.5	20.72	
1.0	$(Mg_{0.21}Fe_{0.79})(Mg_{0.395}Fe_{0.605})_2O_4$	0.794(24)	8.371(73)	4.53	3.63	2.959	−5.1	18.26	29

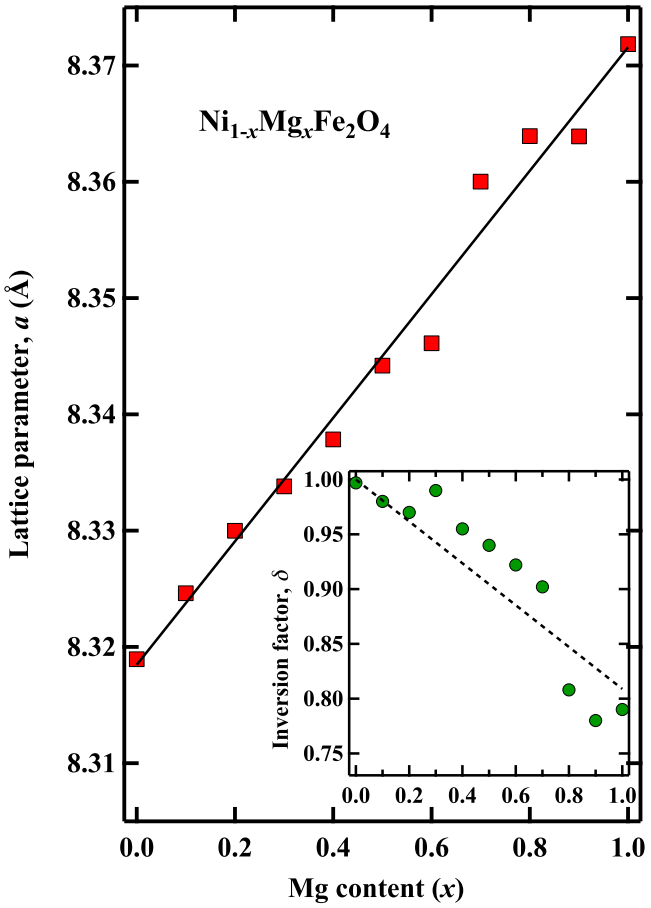

Figure 3. Variation of the lattice constant, a, with the Mg content (x) in $Ni_{1-x}Mg_xFe_2O_4$ nanoparticles with the solid line is the linear fit. The inset shows the variation of the inversion factor $\delta$with x and the dashed line is for guidance.

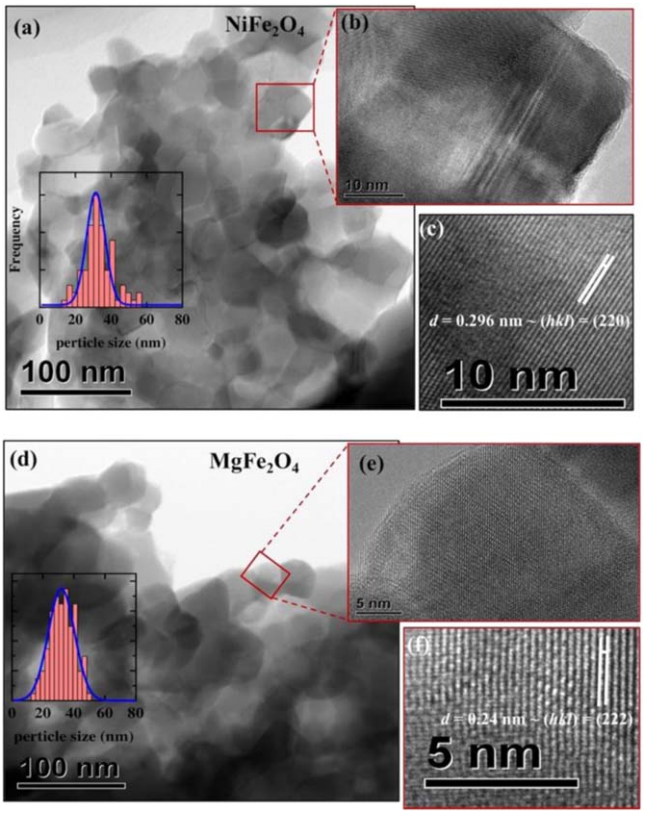

Figure 4. (a) TEM image of $NiFe_2O_4$ nanoparticles, (b) and (c) HRTEM image for one selected particle. (d) TEM image of $MgFe_2O_4$ nanoparticles, (e) and (f) HRTEM image for one selected particle. Insets of (a) and (d) are the estimated particles size distribution for $NiFe_2O_4$ and $MgFe_2O_4$ nanoparticles, respectively.

in figure 3. It is noticeable that the lattice constant linearly increases with Mg-doping from 0.832 nm for $NiFe_2O_4$ to 0.837 nm in a good agreement with Vegard's law [29]. The increase of lattice constant with increasing Mg^{2+} concentration is attributed to the larger size of substituent Mg^{2+} ions (0.072 nm in radius) relative to the replaced Ni^{2+} ions (0.069 nm) [30]. The estimated values are consistent with previously observed values for Ni-Mg ferrite synthesized by a co-precipitation method [31].

Further structural properties such as the theoretical density, ρ_{XRD}, and the hopping lengths (i.e. distance between the magnetic ions) in A and B sublattices, L_A and L_B, which are important factors to the magnetic properties of spinel ferrites, can be estimated from the XRD results of lattice constant a as [32]:

$$\rho_{XRD} = \frac{ZM}{N_A a^3}. \quad (1)$$

Where Z is the number of molecules per unit cell and equal to 8 for spinel ferrites. M is the molecular weight and N_A is the Avogadro's number. The estimated values are presented in table 1 which reveal a gradual decrease of d with increasing Mg concentration. This behaviour is expected due to the substitution of heavier Ni^{2+} by the lighter Mg^{2+} ions as reported previously for Ni–Mg ferrite [31]. L_A and L_B, are estimated as [33] :

$$L_A = \frac{a\sqrt{3}}{4}, \quad L_B = \frac{a\sqrt{2}}{4}. \quad (2)$$

The obtained values of L_A and L_B listed in table 1 show an increase with lattice expansion. The elongated hopping lengths may have influence on the magnetic properties and suggest a decrease of the exchange coupling between magnetic ions by Mg substitution for Ni in $Ni_{1-x}Mg_xFe_2O_4$.

Another interesting result of the Rietveld refinement of the XRD patterns is the indication of cations distribution in a mixed spinel structure close to a completely inversed one. The cation distribution of (A^{IV}) and (B^{VI}) sites for all compositions are listed in table 1. As well-known fact that Ni^{2+} ions prefer octahedral sites [26], the inversion factor is the highest ($\delta = 0.997$) in pure $NiFe_2O_4$ and systematically decreases with substitution with Mg^{2+} for Ni^{2+} ions, as shown in the inset of figure 3. This means that more Mg^{2+} ions replace for Fe^{3+} in the A^{IV}-site and result in slightly reduced inversion with increasing Mg content in $Ni_{1-x}Mg_xFe_2O_4$ nanoparticles which of course has an influence on the magnetic properties [26, 34, 35].

The observed broadening of XRD peaks of the synthesized $Ni_{1-x}Mg_xFe_2O_4$ compositions indicates the reduced

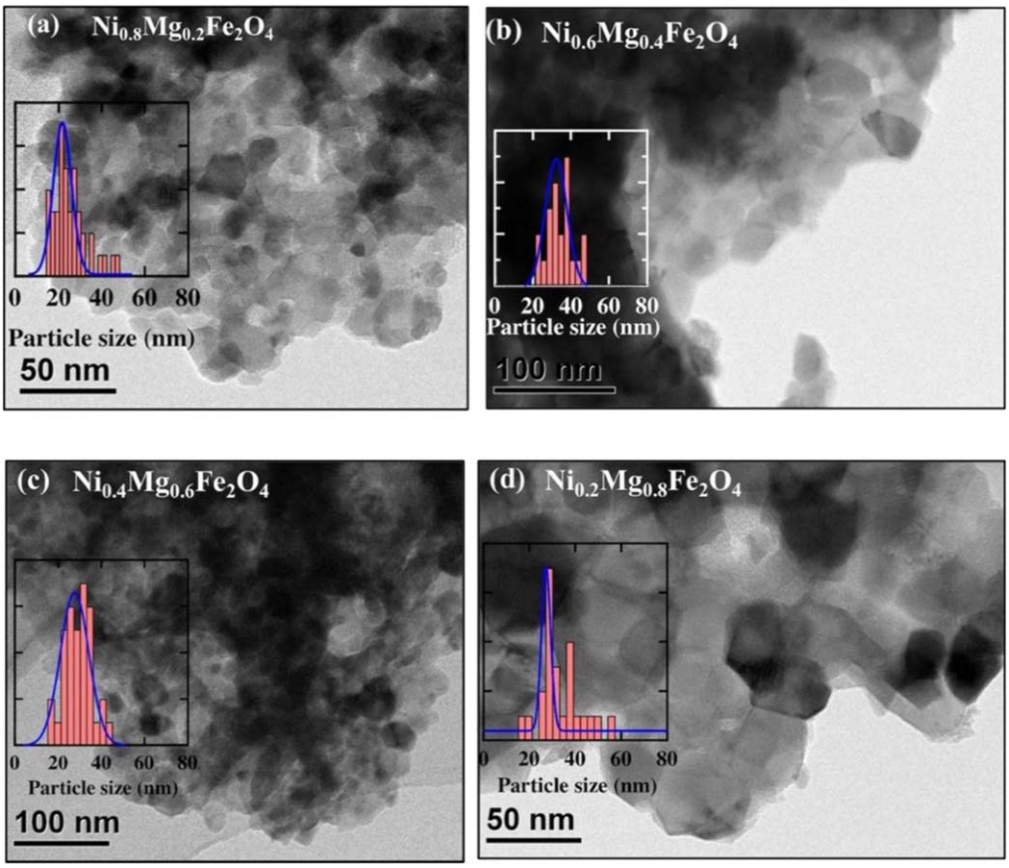

Figure 5. TEM images of solid solution $Ni_{1-x}Mg_xFe_2O_4$ nanocrystals with the estimated particle size distribution shown in the inset of each figure.

crystallite size to a nanoscale. The crystallite size (d_{XRD}) is estimated from the broadening of the XRD peaks obtained using Rietveld refinements and corrected for the internal lattice strain, ε, using the well-known Williamson–Hall formula [36]:

$$\beta \cos\theta = 4\,\varepsilon \sin\theta + \frac{k\lambda}{d_{XRD}}, \tag{3}$$

where k is a constant depends on the shape of the particle and almost equals 0.9, λ is the x-ray wavelength, β is the peak full width at half maximum (FWHM), and θ is the diffraction line Bragg angle. This equation represents a linear relation between $\beta \cos\theta$ (on y-axis) and $\sin\theta$ (on x-axis) from which an intrinsic crystallite size, corrected for the internal strains, can be obtained from the y-axis intersections. The positive slope indicates the presence of tensile strain, while the negative slope shows the presence of compressive strain. The obtained crystallite sizes of the synthesized $Ni_{1-x}Mg_xFe_2O_4$ are presented in table 1. The average crystallite sizes of the microwave-combustion synthesized $Ni_{1-x}Mg_xFe_2O_4$ varies back and forwards between 35 and 18 nm.

3.2. TEM results

The microstructure of the synthesized spinel ferrite nanoparticles, i.e. actual particles size, shape and crystallinity, are studied by transmission electron microscopy (TEM). Figure 4 shows TEM images of the two parent compounds, $NiFe_2O_4$ and $MgFe_2O_4$ nanoparticles with high-resolution transmission electron microscopy (HRTEM). The particles size varies from 15 to 50 nm and its distribution is shown in the insets of figures 4(a) and (d) for $NiFe_2O_4$ and $MgFe_2O_4$, respectively. The crystals shape and size in some selected solid solution samples are shown with the particle size distribution in figure 5. Cubic as well as almost octahedral-shaped crystalline nanoparticles of averages size of about25 – 30 nm are observed. HRTEM images for a selected particle in $NiFe_2O_4$ and $MgFe_2O_4$ nanocrystals are shown in figures 3(b) and (c) for $NiFe_2O_4$ and in (e) and (f) for $MgFe_2O_4$. The single crystalline structure in the selected particles is revealed. Lattice fringes with interfringe distances of 2.95 and 2.4 Å are observed for the selected particle in $NiFe_2O_4$ and $MgFe_2O_4$ which match the d-spacings of the {220}and {222} planes of spinel ferrite, respectively. In agreements with the XRD results of crystal structure and crystallite size, TEM results explore the success to synthesis the targeted spinel ferrite nanocrystals.

3.3. Elemental composition

We have employed the electron dispersive x-ray spectroscopy tool attached to the JEOL TEM microscope (TEM-EDX) to investigate the approximate chemical compositions. Figure 6 shows the TEM-EDX patterns of selected particles in a scanning TEM mode for some samples of $Ni_{1-x}Mg_xFe_2O_4$

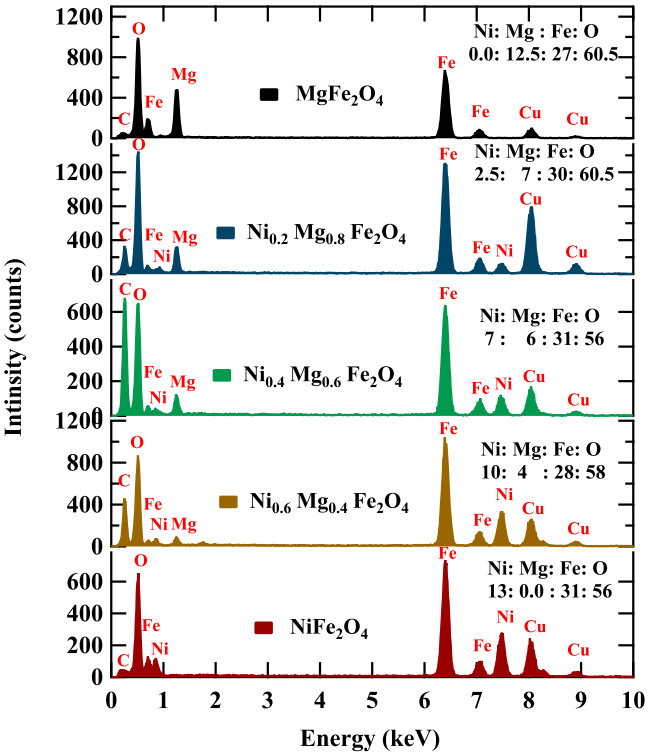

Figure 6. TEM-EDX patterns of the microwave-combustion synthesized $Ni_{1-x}Mg_xFe_2O_4$ nanoparticles.

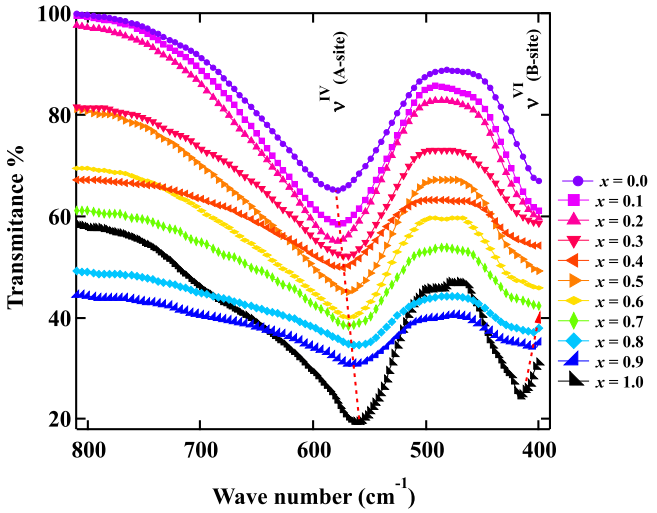

Figure 7. Transmittance FTIR spectra of $Ni_{1-x}Mg_xFe_2O_4$ nanoparticles. The traces are vertically shifted for clarity.

Table 2. FT-IR bands assignment and optical energy gap for $Ni_{1-x}Mg_xFe_2O_4$ nanoparticles.

Mg content (x)	ν^{IV}, ν^{VI} (cm^{-1}) [$\pm$ 2 cm^{-1}]	$E_g^{opt.}$ (eV)
0.0	581	3.61(30)
0.2	579	2.57(46)
0.3	574	2.85(48)
0.4	574	2.49(47)
0.5	570	2.32(58)
0.6	569	2.25(41)
0.7	568	2.16(13)
0.8	564, 402	2.17(24)
0.9	564, 403	1.69(49)
1.0	562, 415	1.63(34)

nanoparticles with the indicated nominal compositions. Some extrinsic peaks of ingredients such as C and Cu in the carbon-coated copper grids of the sample holder are observed. Although the TEM-EDX is not accurate enough compared to SEM-EDX, it reveals a general increase of the Mg on the account of Ni content with approximate ratio of (Mg+Ni) to Fe equals to 1: 2. The average atomic ratio of EDX results for several particles in each sample are indicated in figure 6 for corresponding samples.

3.4. FTIR spectra

In order to investigate the chemical functional groups in the synthesized $Ni_{1-x}Mg_xFe_2O_4$ nanoparticles, FTIR spectroscopy measurements are carried out. The IR transmittance was measured in a range of 400–4000 cm^{-1} and mainly shows the characteristic metal-oxygen vibration bands in its spectra. The spectra are presented in figure 7 in a range of 400–800 cm^{-1}. The two observed essential bands of the M-O bond phonon modes, ν^{IV} in the range 560–580 cm^{-1} corresponding the tetrahedral site and ν^{VI} in the range 395–450 cm^{-1} corresponding octahedral site, are the common FTIR bands observed for spinel ferrites [37]. Unlike the octahedral band frequency ν^{VI}, the tetrahedral one ν^{IV} decreases with increasing Mg content. The variation of band frequency values is due to changes in the bond length at the A^{IV} and B^{VI} sites probably due to varied cations distribution. The tetrahedral site has shorter bond length compared to that of the octahedral site, that is further related to a stronger bonding of Fe^{3+} ions at the A^{IV}-site in the almost inversed spinel structure of Ni-ferrite [38]. In consistence with the results of XRD and Rietveld refinement, the inversion factor δ decreases with Mg-substitution for Ni and hence Fe^{3+} ions gradually emigrate from the A^{IV}-site resulting in rather weak bond and lower ν^{IV}. The low-energy phonon bands coresponding ν^{VI} are not observed for compositions of $x < 0.7$ due to our experiment limitation to 400 cm^{-1}, however, the spectra clearly show the onset of the octahedral bands in these samples. The low-frequency band ν^{VI} has been barely observed for Ni-rich compositions [39, 40]. The band frequencies, ν^{IV} and ν^{VI} observed in the FTIR spectra are listed in table 2.

3.5. Optical properties

The optical properties of Mg-Ni ferrite nanocrystals are studied by analysing the measured UV-Visible absorbance. The optical band gap can be estimated according to the well-known Tauc's relation [41]:

$$\alpha h\nu = \beta(h\nu - E_g^{opt.})^m. \quad (4)$$

Where α is the absorption coefficient,ν is the frequency of the incident light, h is planks constant and $E_g^{opt.}$ is the optical energy gap. The m exponent can take the values of 2, 3, 1/2,

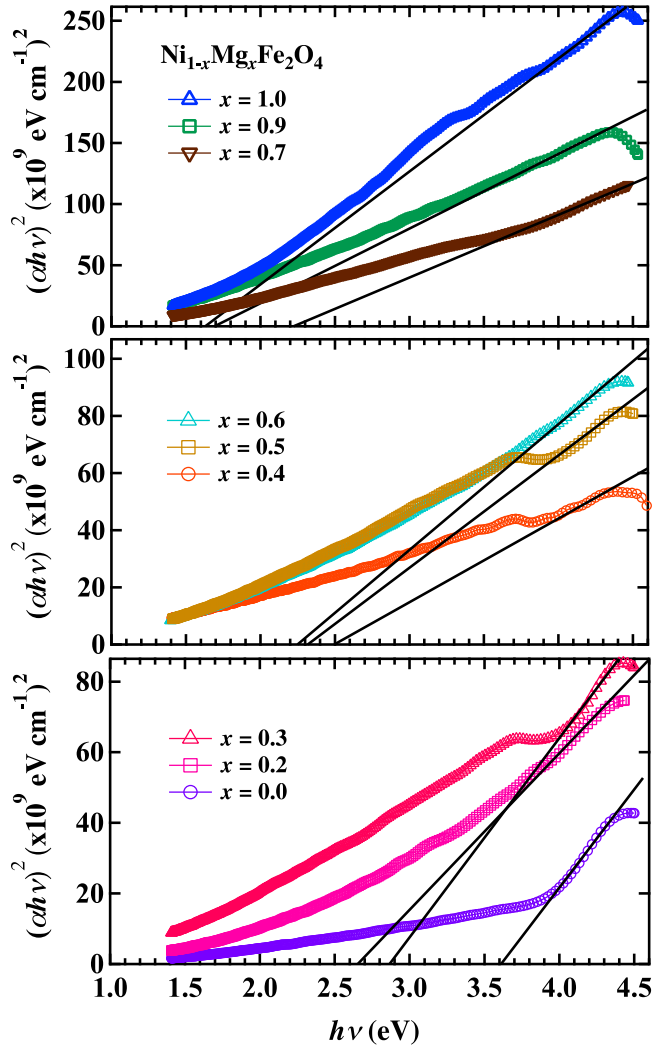

Figure 8. Tauc's plots of the UV-visible optical absorbance data of $Ni_{1-x}Mg_xFe_2O_4$ nanoparticles. Inset shows optical energy gap determination.

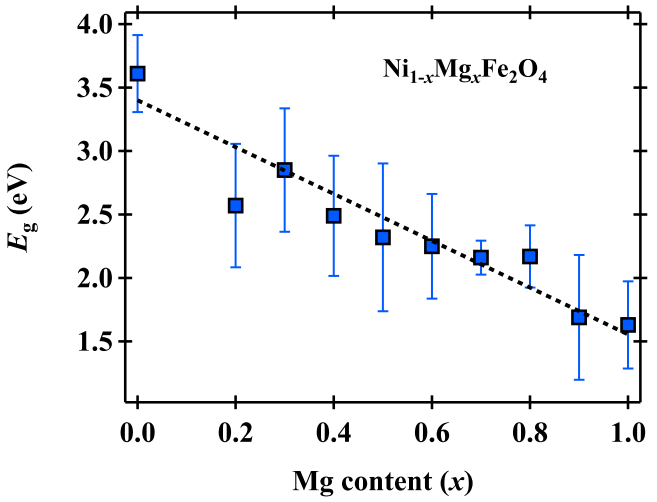

Figure 9. The variation of the optical energy gap, E_g, versus Mg content (x) in $Ni_{1-x}Mg_xFe_2O_4$ nanoparticles. Dashed line is linear fit presented for guidance.

3/2, for transitions described as indirect allowed, indirect forbidden, direct allowed and direct forbidden transition, respectively.

After plotting the $(\alpha h\nu)^{1/m}$ against the incident photon energy $h\nu$ for different values of the exponent m, we found that the best linear divergence of Tauc's plot occurs for $m = 1/2$ indicating optical band gap of a direct allowed transition type in $Ni_{-x}Mg_xFe_2O_4$ nanoparticles, that agree with results previously reported for spinel ferrites [22, 39, 42]. Figure 8 shows the Tauc plots, $(\alpha\ h\nu)^2$ versus the incident photon energy ($h\nu$), for $Ni_{-x}Mg_xFe_2O_4$ nanoparticles of differnt x. The optical band gap ($E_g^{opt.}$) is obtained by extrapolating the mostly divergent linear portion of the Tauc plot to $(\alpha h\nu)^2 = 0.0$, as presented in figure 8 by the solid lines. The obtained values of $E_g^{opt.}$ are listed in table 2 and its compositional dependence is shown in figure 9. The obtained data reveal that the optical band gap decreases from 3.61(30) for Ni-ferrite to 1.63(34) eV for Mg-ferrite and is almost lineally tuneable in between by changing Mg concentration, in the uncertainty limits as shown by the dashed line, which is atributed to the change in the electronic structure. Similar behavior of E_g with the Mg content has been reported for Mg-Zn ferrites prepared by a microwave combustion method [42].

The slight differences in the band gap of $Ni_{1-x}Mg_xFe_2O_4$ nanoparticles from previous bulk studies may be attributed to quantum confinment effects and the formation of sub-band gap energy levels that are induced by the abundant surface and interface defects in the agglomerated nanoparticles [43]. The red shift for E_g from bulk values that increases with Mg incorporation could also be attributed to an increase in the internal lattice strain as reported in the earlier publication by S. Singh *et al* [44], where the optical band gap of $CoFe_2O_4$ was found to decrease from 1.84 to 1.67 eV with increasing the intrinsic strain.

4. Conclusion

$Ni_{1-x}Mg_xFe_2O_4$ nanoparticles were successfully synthesized in the whole range of $0.0 \leqslant x \leqslant 1.0$ by a microwave-assisted combustion route using a glycine fuel. Characterization measurements by XRD, FTIR, TEM and EDX techniques confirm the spinel structured ferrite nanocrystals with crystalline correlation lengths of 20–40 nm that is comparable to the particle size observed by TEM. High-resolution TEM indicated the high crystallinity in the synthesized nanocrystals. Rietveld refinement of the XRD patterns resulted in a lattice constant of 0.8318 nm for $NiFe_2O_4$ that linearly increases with Mg^{2+} substitution for the smaller Ni^{2+} ions. Cations distribution in a highly inversed spinel structure has been revealed with an inversion factor that decreases with Mg^{2+} substitution for Ni^{2+}. Analysis of the measured optical absorbance spectra has indicated a wide-to-narrow energy gap tuning by Mg substitution for Ni.

Acknowledgments

The authors gratefully acknowledge the financial support unit at the Faculty of Science, Assiut University (Egypt) for the support under grant number 4-1-2019. Authors would like to thank Mr N. Sasaki and Mr K. Kazumi from the Department of Materials Science and Engineering, Kyoto University (Japan) for assistance and discussion in the TEM results.

ORCID iDs

Abdulaziz Abu El-Fadl https://orcid.org/0000-0003-2413-5965
Mohamed A Kassem https://orcid.org/0000-0001-8871-6078

References

[1] Amiri M, Salavati-niasari M and Akbari A 2019 Magnetic nanocarriers : evolution of spinel ferrites for medical applications *Adv. Colloid Interface Sci.* **265** 29–44
[2] Qu J, Che T, Shi L, Lu Q and Qi S 2019 A novel magnetic silica supported spinel ferrites $NiFe_2O_4$ catalyst for heterogeneous Fenton-like oxidation of rhodamine B *Chinese Chem. Lett.* **30** 1198–203
[3] Javed H, Rehman A, Mussadiq S, Shahid M and Azhar M 2019 Reduced graphene oxide-spinel ferrite nano-hybrids as magnetically separable and recyclable visible light driven photocatalyst *Synth. Met.* **254** 1–9
[4] Maksoud M I A A *et al* 2019 Antibacterial, antibiofilm, and photocatalytic activities of metals-substituted spinel cobalt ferrite nanoparticles *Microb. Pthogenes.* **127** 144–58
[5] Amiri M, Eskandari K and Salavati-niasari M 2019 Magnetically retrievable ferrite nanoparticles in the catalysis application *Adv. Colloid Interface Sci.* **271** 101982
[6] Niaz M *et al* 2017 Evaluation of structural, morphological and magnetic properties of switching and MLCI's applications *J. Magn. Magn. Mater.* **421** 260–8
[7] Chand J, Verma S and Singh M 2013 Structural, magnetic and Mössbauer spectral studies of Sm^{3+} ions doped Mg ferrites synthesized by solid state reaction technique *J. Alloys Compd.* **552** 264–8
[8] Ajmal M, Islam M U, Ashraf G A, Nazir M A and Ghouri M I 2017 The influence of Ga doping on structural magnetic and dielectric properties of NiCr0.2Fe1.8O4 spinel ferrite *Phys. B Condens. Matter* **526** 149–54
[9] Sanpo N, Berndt C C, Wen C and Wang J 2013 Transition metal-substituted cobalt ferrite nanoparticles for biomedical applications *Acta Biomater.* **9** 5830–7
[10] Javed H, Iqbal F, Olaleye P and Azhar M 2019 Structural, electrical and magnetic parameters evaluation of nanocrystalline rare earth Nd^{3+} -substituted nickel-zinc spinel ferrite particles *Ceram. Int.* **45** 11125–30
[11] Babu K V, Satyanarayana G, Sailaja B, Kumar G V S, Jalaiah K and Ravi M 2018 Results in physics structural and magnetic properties of Ni0. 8 $M_{0.2}Fe_2O_4$ (M = Cu, Co) nano-crystalline ferrites *Results Phys.* **9** 55–62
[12] Sartaj H, Ali R, Shah F, Ismail B and Nisar J 2019 Improved electrical, dielectric and magnetic properties of Al-Sm co-doped $NiFe_2O_4$ spinel ferrites nanoparticles *Mater. Sci. Eng. B* **243** 47–53
[13] Gupta N, Jain P, Rana R and Shrivastava S 2017 Current development in synthesis and characterization of nickel ferrite nanoparticle *Mater. Today Proc.* **4** 342–9
[14] Isaac B T, Assunção A G D, De Oliveira J B L and De Holanda S M 2019 Efficiency estimative and characterization of nickel ferrite nanoparticles produced by sol-gel modified by ICR cross-linked technique *Mater. Lett.* **254** 13–6
[15] Umut E, Cos M, Pineider F, Berti D and Güngünes H 2019 Nickel ferrite nanoparticles for simultaneous use in magnetic resonance imaging and magnetic fluid hyperthermia *J. Colloid Interface Sci.* **550** 199–209
[16] Nandan B, Bhatnagar M C and Kashyap S C 2019 Cation distribution in nanocrystalline cobalt substituted nickel ferrites : x-ray diffraction and Raman spectroscopic investigations *J. Phys. Chem. Solids* **129** 298–306
[17] Udhaya P A, Bessy T C and Meena M 2019 Antibacterial activity of nickel and magnesium substituted ferrite nanoparticles synthesized via self-combustion method *Mater. Today Proc.* **8** 169–75
[18] Hao A, Jia D, Ismail M, Chen R and Bao D 2019 Controlling of resistive switching and magnetism through Cu^{2+} ions substitution in nickel ferrite based nonvolatile memory *J. Alloys Compd.* **790** 70–7
[19] Slimani Y *et al* 2019 Effect of bimetallic (Ca, Mg) substitution on magneto-optical properties of $NiFe_2O_4$ nanoparticles *Ceram. Int.* **45** 6021–9
[20] Chandra Babu Naidu K and Madhuri W 2017 Microwave processed bulk and nano NiMg ferrites: a comparative study on x-band electromagnetic interference shielding properties *Mater. Chem. Phys.* **187** 164–76
[21] Nadumane A, Shetty K, Anantharaju K S, Nagaswarupa H P, Rangappa D and Vidya Y S 2019 Sunlight photocatalytic performance of Mg-doped nickel ferrite synthesized by a green sol-gel route *J. Sci. Adv. Mater. Devices* **4** 89–100
[22] Shobana M K, Kim K and Kim J 2019 Impact of magnesium substitution in nickel ferrite: optical and electrochemical studies *Phys. E Low-dimensional Syst. Nanostructures* **108** 100–4
[23] Liu H, Li A, Ding X, Yang F and Sun K 2019 Magnetic induction heating properties of $Mg_{1-x}Zn_xFe_2O_4$ ferrites synthesized by co-precipitation method *Solid State Sci.* **93** 101–8
[24] Shen W, Zhang L, Zhao B, Du Y and Zhou X 2018 Growth mechanism of octahedral like nickel ferrite crystals prepared by modified hydrothermal method and morphology dependent magnetic performance *Ceram. Int.* **44** 9809–15
[25] Rahimi M, Eshraghi M and Kameli P 2014 Structural and magnetic characterizations of Cd substituted nickel ferrite nanoparticles *Ceram. Int.* **40** 15569–75
[26] Abu El-Fadl A, Hassan A M, Mahmoud M H, Tatarchuk I P, Yaremiy T, Gismelssed A M and Ahmed M A 2019 Synthesis and magnetic properties of spinel $Zn_{1-x}Ni_xFe_2O_4$ ($0.0 \leqslant x \leqslant 1.0$) nanoparticles synthesized by microwave combustion method *J. Magn. Magn. Mater.* **471** 192–9
[27] Izumi F, Momma K, Izumi K and Momma F 2007 Three-dimensional visualization in powder diffraction *Solid State Phenom.* **130** 15–20
[28] Nelson J B and Riley D P 1945 An experimental investigation of extrapolation methods in the derivation of accurate unit-cell dimensions of crystals *Proc. Phys. Soc.* **57** 160–75
[29] Vegard L 1921 Die Konstitution der Mischkristalle und die Raumfüllung der Atome *Zeitschrift für Phys.* **5** 17–26
[30] Shannon R D 1976 Revised effective ionic radii and systematic studies of interatomic distances in halides and chalcogenides *Acta Crystallogr. Sect.* A **32** 751–67
[31] Naeem M, Shah N A, Gul I H and Maqsood A 2009 Structural, electrical and magnetic characterization of Ni-Mg spinel ferrites *J. Alloys Compd.* **487** 739–43

[32] Zak A K, Abrishami M E, Majid W H A, Yousefi R and Hosseini S M 2011 Effects of annealing temperature on some structural and optical properties of ZnO nanoparticles prepared by a modified sol-gel combustion method *Ceram. Int.* **37** 393–8

[33] Viswanathan B and Murthy V R K 1990 *Ferrite Materials: Science and Technology* (Berlin: Springer)

[34] Sijo A K 2017 Influence of fuel-nitrate ratio on the structural and magnetic properties of Fe and Cr based spinels prepared by solution self combustion method *J. Magn. Magn. Mater.* **441** 672–7

[35] Sijo A K, Jha V K, Kaykan L S and Dutta D P 2019 Structure and cation distribution in superparamagnetic $NiCrFeO_4$ nanoparticles using Mössbauer study *J. Magn. Magn. Mater.* **497** 166047

[36] Williamson G K and Hall W H 1953 X-ray line broadening from filed aluminum and wolfram *Acta Metall.* **1** 22

[37] Hussain M, Meydan T, Cuenca J A, Melikhov Y and Mustafa G 2018 Microwave absorption properties of CoGd substituted $ZnFe_2O_4$ ferrites synthesized by co-precipitation technique *Ceram. Int.* **44** 5909–14

[38] Mahmoud M H 2012 Infrared investigations of Cu-Zn ferrite substituted with rare earth ions R = Nd *Mater. Lett.* **73** 226–8

[39] Srivastava M, Ojha A K, Chaubey S and Materny A 2009 Synthesis and optical characterization of nanocrystalline $NiFe_2O_4$ structures *J. Alloys Compd.* **481** 515–9

[40] Berchmans L J, Selvan R K, Kumar P N S and Augustin C O 2004 Structural and electrical properties of $Ni_{1-x}Mg_xFe_2O_4$ synthesized by citrate gel process *J. Magn. Magn. Mater.* **279** 103–10

[41] Kannan Y B, Saravanan R, Srinivasan N and Ismail I 2017 Sintering effect on structural, magnetic and optical properties of $Ni_{0.5}Zn_{0.5}Fe_2O_4$ ferrite nano particles *J. Magn. Magn. Mater.* **423** 217–25

[42] Manikandan A, Vijaya J J, Sundararajan M, Meganathan C, Kennedy L J and Bououdina M 2013 Optical and magnetic properties of Mg-doped $ZnFe_2O_4$ nanoparticles prepared by rapid microwave combustion method *Superlattices Microstruct.* **64** 118–31

[43] Manikandan A, Judith Vijaya J, John Kennedy L and Bououdina M 2013 Microwave combustion synthesis, structural, optical and magnetic properties of $Zn_{1-x}Sr_xFe_2O_4$ nanoparticles *Ceram. Int.* **39** 5909–17

[44] Singh S and Khare N 2018 Effect of intrinsic strain on the optical bandgap and magnetic properties of single domain $CoFe_2O_4$ nanoparticles *Appl. Phys.* A **124** 1–7